AIAA JOURNAL
Vol. 31, No. 10, October 1993

Low Aspect Ratio Wing Code Validation Experiment

Michael E. Olsen* and H. Lee Seegmiller†
NASA Ames Research Center, Moffett Field, California 94035

A code validation experiment for transonic flow is described. The experimental geometry is a low aspect ratio wing, tested in a solid wall wind tunnel. Inflow conditions were measured far enough upstream of the model to allow simple specification. Experimental uncertainties are given for pressure, temperature, velocity, and position measurements, as well as bounds on model deflections and transition location. Cursory comparison with simple computational models provides a baseline of flow conditions that should be readily modeled as well as denotes those cases that will be more challenging. The data include a wide range of α, M_∞, and two Re_{c_r}. The Reynolds numbers reached in this experiment reproduce those experienced by an aircraft with a 5-m root chord, flying at 14–16 km, from Mach 0.6 to 0.8. The angle-of-attack range of the experiment extends into the regime of leading-edge separation (0 deg $\leq \alpha \leq$ 8 deg).

Nomenclature

a = local speed of sound
a^* = sound speed at sonic conditions
$b/2$ = semispan of wing
C_p = coefficient of pressure, $(p - p_\infty)/q_\infty$
c = local wing chord (a function of η)
c_r = wing root chord
c_t = wing tip chord
M_∞ = freestream Mach number
M_∞^{crit} = lowest M_∞ at which sonic flow is attained at some point in the flowfield
p_t = total (pitot) pressure measured at $\xi_0 = -2.25$, $\eta = 1.6$, and $\zeta = 0$
p_∞ = static pressure measured at $\xi_0 = -2.525$, $\eta = 1.6$, and $\zeta = 0$
q_∞ = freestream dynamic pressure ($\frac{1}{2}\rho U_\infty^2$)
Re_{c_r} = Reynolds number based on root chord ($U_\infty c_r/\nu$)
T_t = freestream total temperature, measured in stagnation chamber
u = axial velocity
v = spanwise velocity
w = vertical velocity
x = axial position, origin at wing root leading edge (see Fig. 2)
y = spanwise position, origin at wing root leading edge (see Fig. 2)
z = vertical position (normal to xy plane), origin at wing root leading edge (see Fig. 2)
ζ = vertical distance normalized by c_r, z/c_r
η = spanwise distance, normalized by $b/2$, $2y/b$
ν = kinematic viscosity
ξ = axial distance from leading edge, normalized by local wing chord, $[x - x_{le}(\eta)]/c(\eta)$
ξ_0 = axial distance from root leading edge, normalized by root chord, $[x - x_{le}(0)]/c_r$
ρ = mass density

Subscripts and Superscripts

$c/4$ = wing quarter chord
le = wing leading edge
t = total (stagnation) conditions upstream of wing
te = wing trailing edge
∞ = static conditions at $\xi_0 = -2.525$
$*$ = sonic conditions

Introduction

THIS experiment is one of the benchmark NASA computational fluid dynamics (CFD) validation experiments.[1,2] The validation of codes and the development of turbulence models are pacing the use of CFD, and this experiment is designed to address these issues. This experiment models realistic flight conditions that can be controlled by viscous (turbulence) physics. Low aspect ratio wings are common in modern day fighter aircraft. These aircraft operate at transonic Mach numbers, and with shock boundary-layer interactions and leading-edge vortices, Reynolds number plays a major role in the aerodynamics of these aircraft.

This experiment has been conceived and executed as a code validation experiment. Several steps have been taken to simplify the experiment in the interest of code validation. The wing has no camber, dihedral, or twist, providing symmetry checks and simplifying the CFD gridding process. The experiment has been conducted in a closed-wall test section. The solid walls can be readily modeled computationally, whereas porous walls cannot. The fidelity of the modeling can be assessed, and if necessary improved (e.g., adding viscous terms in zones near the wing). Wall static pressures and inlet boundary-layer measurements were taken along with the wing surface static pressure to provide the boundary conditions necessary for codes ranging from panel methods to time-averaged Navier-Stokes.

This paper will discuss the wing and wall static pressure measurements, tunnel boundary-layer total pressure measurements, and inflow laser Doppler anemometer (LDV) profile data obtained on the wing-alone configuration in the Ames High Reynolds Channel II. The test conditions range from subcritical to supercritical ($0.6 \leq M_\infty \leq 0.8$). Two Reynolds numbers have been investigated, nominally 7×10^6 and 14×10^6 based on root chord. The symmetric model was run at angles of attack of 0, ± 2, ± 5, and ± 8 deg, which includes the regime of leading-edge separation.

Description of Experiment

Experimental Model

The model shown in Fig. 1 was designed with the help of CFD codes, notably TWING,[3] a transonic full potential code.

Presented as Paper 92-0402 at the AIAA 30th Aerospace Sciences Meeting, Reno, NV, Jan. 6–9, 1992; received Jan. 17, 1992; revision received Dec. 28, 1992; accepted for publication Dec. 31, 1992.

*Research Scientist, Modelling and Validation Branch. Senior Member AIAA.
†Research Scientist, Modelling and Validation Branch.

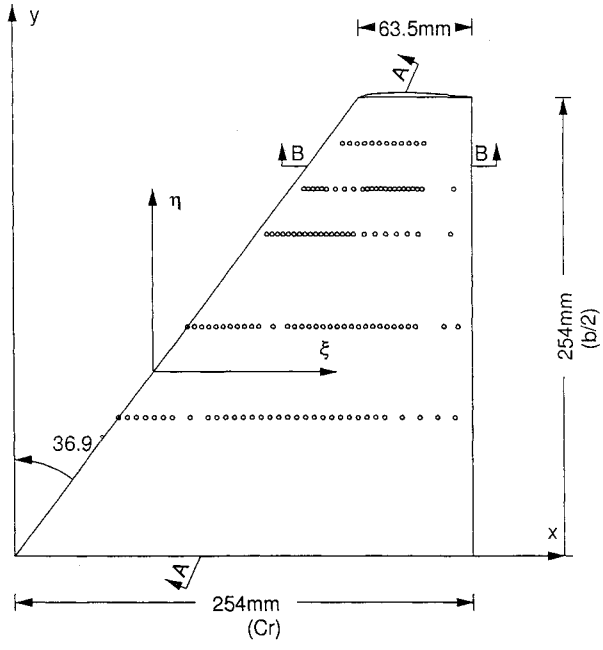

Fig. 1a Wing planform.

Fig. 1b NACA 64A010 airfoil.

The location of the pressure taps on the wing was guided by calculations made with TWING, and the shock location was resolved relatively well in the actual experiment based on the pressure tap spacing chosen with the help of this code.

The geometry studied in this experiment is a semispan low aspect ratio wing. The root chord of the wing c_r is 254 mm, and this dimension is used throughout this paper as the fundamental unit of length. The tip chord c_t is $0.25c_r$. The root and tip chord lines are aligned with the freestream direction. The semispan of the wing $(b/2)$ is $1.0c_r$. The leading and trailing edges of the wing are straight line segments, and the equations defining them are

$$x_{le} = (0.75c_r)\eta \tag{1}$$

$$x_{te} = c_r \tag{2}$$

The wing is untwisted and has no dihedral. A diagram of the wing planform is shown in Fig. 1, and the planform parameters are listed in Table 1.

The cross section of the wing in the xz plane is the NACA 64A010 airfoil (Fig. 1). The airfoil ordinates were obtained using Ref. 4, and the output of this code was checked using Ref. 5 (note that Ref. 5 has an error in the 7.5% chord ordinate).

The tip geometry is unique. If the wing is cut in a constant ξ plane, the wing thickness decreases linearly from root to tip since the airfoil section is identical, and the chord decreases linearly. The lower and upper surface are joined at the tip, $\eta = 1$, by the circular arc that is tangent to both the upper and lower surface. The crucial difference is that the arc lies in a constant ξ plane, as opposed to a constant x plane, avoiding a slope discontinuity at the junction of the wing tip and the leading edge. This tip definition provides a well-defined and easily gridded wing surface without slope discontinuities.

Since the airfoil section used is symmetric and the wing has no twist or dihedral, the entire model is symmetric about the xy plane, hereafter referred to as the wing reference plane. The xy symmetries of the model allowed an experimental check on the overall fidelity of the experimental measurements.

Table 1 Wing planform parameters

Γ	0.0	Wing dihedral, deg
α_g	0.0	Wing geometric twist, deg
Λ_{le}	36.9	Leading-edge sweep, deg
$\Lambda_{c/4}$	29.357	Quarter-chord sweep, deg
Λ_{te}	0.0	Trailing-edge sweep, deg
λ	0.25	Taper ratio, (c_t/c_r)
AR	3.2	Aspect ratio, (b^2/S)
$\bar{c}$	$0.7c_r$	Mean aerodynamic chord

As the desired conditions include high angle of attack, the structural integrity of the model was a major consideration. The model was of two-piece construction, using a lower surface hatch for access to the pressure taps during construction and a continuous upper surface for adequate bending stiffness. Along with the use of a high-strength steel, this reduced the structural deflection of the model under the high loads it experienced during the test.

The wing is instrumented with 132 pressure taps, 128 of which are on its upper surface. These are located along five spanwise strips: $\eta = 0.3$, 0.5, 0.7, 0.8, and 0.9. Four additional taps are located on the lower surface of the wing. These provide a symmetry check and a means of defining the aerodynamic zero angle of attack. Two of these taps are located along $\eta = 0.3$, at $\xi = 0.2$ and 0.5, and the other two are located along $\eta = 0.5$ at $\xi = 0.2$ and 0.5.

The 250-μm $(0.001c_r)$ diam pressure taps were created via an electrodischarge machining (EDM) process, which ensures clean orifice shoulders, and are perpendicular to the local normal of the wing surface. The entire wing was machined using numerically controlled machining, and the finished product was within 100 μm $(0.0004c_r)$ in thickness of that specified over the entire wing. The nominal error over the sections inspected (root and tip) was below 25 μm $(0.0001c_r)$.

The surface finish of the wing was specified as $\sqrt{64}$, which would imply an allowable surface roughness of 1.6 μm $(6.4\times10^{-6}c_r)$, but the wing actually had a mirror finish. Following an inadvertent two-phase flow experiment following the breakup of an upstream control valve, the surface roughness of the wing was measured. On the upper surface, the surface roughness was less than 0.1 μm $(400\times10^{-9}c_r)$, the lowest value of roughness the profilometer could measure. On the portion of the wing that greeted the valve fragments as they moved downstream, 12 mm $(0.05c_r)$ from the leading edge of the wing, the roughness was below 0.5 μm $(2\times10^{-6}c_r)$. It was not possible to obtain a reading closer to the leading edge than this.

Experimental Facility

The experimental program was conducted at the NASA Ames Research Center in the High Reynolds Channel II facility, shown in Fig. 2 and described in detail in Ref. 6. This blowdown facility has a solid wall test section, with a 0.406×0.609 m $(1.6c_r\times2.4c_r)$ nominal test section area. Given the geometry of the wing, this implies a blockage based on projected frontal area less than 0.017.

The high Reynolds numbers are produced by running at conditions of high p_t, as opposed to lowering T_t. The total pressures obtained in this set of runs reached 3.3 atm absolute, and the total temperatures ranged between 250 and 260 K. The run times for this test were chosen to include at least 45 s of constant conditions for data acquisition, for the mean surface pressure measurements. The laser Doppler anemometer data runs were conducted over longer times, some over 2 min.

The facility has flexible upper and lower walls so that "free air" conditions can be approximated for two-dimensional models. For this test, the upper and lower walls were diverged at a half-angle of 0.11 deg from the tunnel centerline to accommodate boundary-layer growth and produce $\partial p/\partial x = 0$ with the tunnel empty. The flexible walls exhibit small waviness due to the nature of their construction. The maximum amount of

variation in tunnel height across the tunnel was below 1 mm ($0.004c_r$). The variation in the tunnel width is below this amount. This implies that the cross section deviation from right angles was less than 0.15 deg.

No wind-tunnel boundary-layer suction was used during this test. The tunnel wall boundary layers were measured with two total pressure rakes. The freestream turbulence level of the tunnel has been reported as 0.005 (u'/U_∞), consistent with the laser Doppler anemometer results obtained during the course of the test.

Measurement Instrumentation

Pressure Measurement System

The cornerstone of the pressure measurement system was a dead weight tester, used to calibrate all pressure transducers. The device is capable of producing pressures known to 100 ppm. The device was verified to be within this specification of accuracy (tracable to NBS standards) during the course of this experiment. With the uncertainty of the estimate of the local value of the acceleration due to gravity, obtained from the U.S. Geological Survey, the pressures produced were known to within 250 ppm.

The dead weight tester was used to calibrate secondary pressure standards used during the test, which were barocel pressure transducers. These transducers were calibrated frequently with the dead weight tester throughout the test and compared against each other as a check on their accuracy. These transducers were mounted on heaters and insulated for temperature stabilization. These transducers were also used to measure the two most critical pressures, p_t and p_∞. The accuracy of the barocel measurements was better than 0.0005 (500 ppm) of p_t.

The remaining pressure measurements were obtained with electronically scanned transducers. These were calibrated using the barocel pressure transducers as a secondary standard at the start of each wind-tunnel run and were (like the barocels themselves) also mounted on heaters and insulated to stabilize their temperatures. These transducers were referenced directly to p_∞ during the run and thus measure the value $p - p_\infty$ directly.

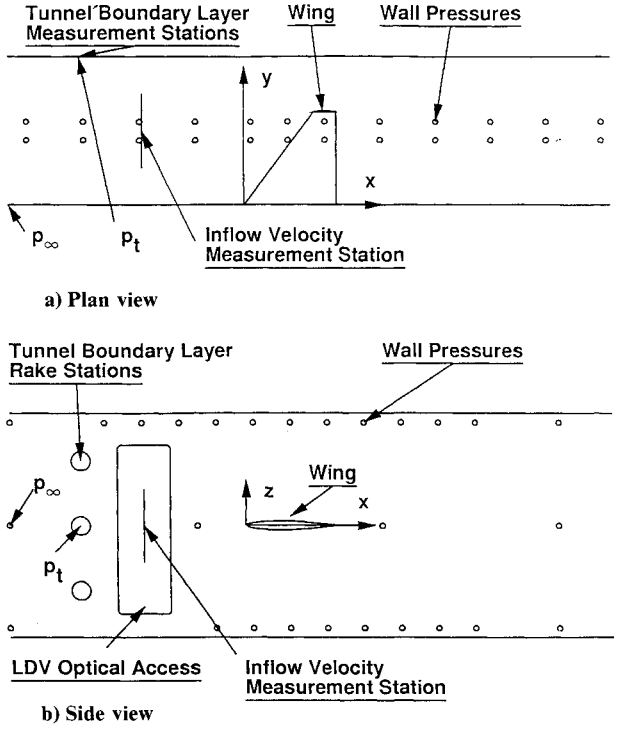

Fig. 2 Diagram of HRC-II wind tunnel showing instrumentation.

Temperature Measurement

The total temperature was measured using iron-constantin (type J) thermocouples. These were located upstream of the model, affixed to screens in the settling chamber. Three thermocouples were used to provide the T_t measurement. The voltages were amplified at a gain of 500, and the amplifiers and thermocouples were monitored daily. With the three measurements of T_t the thermocouples provided another internal check in the measurements, similar to that provided by the two barocels.

Velocity and Position Measurement

The laser Doppler anemometer measurements were obtained with a two-component LDV, described in Ref. 7. This system measures the streamwise and vertical velocities at selected locations in the flowfield. The LDV system was employed to measure inflow velocities of $1.775c_r$ ahead of the wing root leading edge ($\xi_0 = -1.775$) to evaluate the inflow uniformity.

This system was also employed to measure the wing bending during the run. A laser beam was split by the wing trailing edge. The difference in position to obtain the same light pattern with flow and no flow in the wind tunnel yielded a measurement of the displacement of the wing at the point at which the laser beam intersected the wing.

Accuracy Evaluation

The accuracy of this data set is of primary importance, since it will be used as a standard for the evaluation of CFD codes. The error analysis of the data set includes the accuracy of the standards used to calibrate the devices, the statistical uncertainty of the individual measurements, and the drift of the instruments used in the measurements. When possible, instruments were used as internal checks on each other, as in the case of the thermocouple, barocel pressure, and LDV measurements.

Pressure Measurements

The accuracy of the pressure measurements on the wing surface is controlled by more than simply the accuracy of the transducer measurements. The dominant sources of inaccuracy in the pressure measurements were produced by the effects of finite hole size[8] and by geometric imperfections in the tunnel walls. The accuracy of the pressure measurement process itself was insignificant with respect to these two effects. Unfortunately, these effects introduce an error that can only be estimated and not measured directly in a "single sample" experiment.

The effect of finite hole size is associated with the level of shear stress at the surface of the wing. The surface shear stress can increase the pressure in the pressure tap above the static pressure at the wing surface. Since the geometry of the taps is given, the effect of finite hole size/local shear can be estimated if the wing surface shear level can be estimated. Since this may not be the case (for instance, one may desire to validate an Euler solver or transonic panel method), and the accuracy of the correction would depend on the accuracy of the surface shear estimate, the effect of finite hold size is included in the assessment of accuracy of the C_p values. For the conditions of this test, this can produce an elevation of C_p by 0.04 close to the leading edge. For the portions of the wing at which the surface shear is equal to or less than the average surface shear, the correction should be less than 0.01 in C_p.

Disturbances produced by imperfections in the wind-tunnel walls also affect the overall accuracy of the measurements. The overall influence of the walls is not included here as an inaccuracy, since this can be readily modeled by the flow codes, given that the walls are solid, and hence a simple no-flow boundary condition. The symmetry of the model and the wind-tunnel configuration allow an assessment of the level of this source of inaccuracy. Using the C_p measurements on opposite sides of the wing and tunnel to estimate the effect of the tunnel imper-

fections on the values of C_p, this source of error was less than 0.01 in C_p for the conditions of this test.

For the C_p measurements, the bias (introduced by the effect of hole size) in these measurements is less than 0.04 on the wing surface, and the random error (or precision) is less than 0.01, caused by the imperfections of the wind-tunnel facility. Other sources of error are negligible compared with these effects. These other negligible sources include calibration inaccuracies ($\leq$200 ppm), transducer drift ($\leq$100 ppm), and statistical error ($\leq$200 ppm). The internal consistency of the pressure data when the transducers were measuring a known pressure or two transducers measured identical pressures was $\leq$200 ppm, and this was monitored during the course of the test to detect and track down leaks and electrical malfunctions.

Temperature Measurements

The temperature measurements were accurate to 3°C. The differences between the thermocouple measurements were included in the uncertainty estimate of this quantity. At the temperatures encountered in this test, this results in an uncertainty in a^* of $\pm$0.5% and in a contribution of 0.01 Re_{c_r} to the uncertainty in the Reynolds number. This contributes over 90% of the uncertainty in the estimate of U_∞, again 0.5%.

Velocity Measurements

The laser Doppler anemometer system measurements are accurate to 0.5% in magnitude and 1 deg in angle. The velocities measured with this system are normalized by the sound speed or alternately with the freestream velocity determined from the freestream Mach number and the total temperature. The relative inaccuracies of all systems involved come into play, with the laser Doppler anemometer and T_t errors predominating. With the assumption that the errors of the p_t, p_∞, T_t, and velocity measurement systems are independent, the overall accuracy level of the v/a^* or v/U_∞ measurements becomes 1%. This level of accuracy is borne out by the variation in velocity measured during the course of a run, the repeatability of measurements between runs, and laser Doppler anemometer alignments.

The experimental uncertainties were monitored by identical measurements conducted at the beginning and end of the tunnel runs, as well as measurements made at the same location over multiple runs and multiple setups. This practice should indicate the effects of temperature drift, as well as calibration inaccuracies in the laser Doppler anemometer setup.

The determination of the location of the measuremnt volume is accurate to 0.13 mm (0.0005c_r) in the x and z dimensions. The measurement volume size is less than 11.7 mm (0.046c_r) spanwise and 0.275 mm (0.001c_r) in the x-z plane, to the e^{-2} point.

Boundary Condition Results

The boundary conditions measured during the course of the test are those that are necessary and sufficient to completely specify the flowfield for a time-averaged Navier-Stokes code. Ambiguity in the boundary conditions translates directly into ambiguity in the flowfield, making this is an important point for validation experiments. The test section has solid walls, and hence inflow Mach and Reynolds numbers as well as outflow C_p conditions must be specified. If the inflow velocity is nonuniform, for any reason, the distribution of magnitude and direction of the incoming flow must also be specified. If the tunnel is to be modeled using viscous tunnel walls, specification of the incoming velocity distributions in the tunnel wall boundary layer is also necessary.

Tunnel Wall Boundary Layer

The incoming tunnel wall boundary layer was measured with two total pressure rakes: one at $\xi_0 = -1.8$, $\eta = 0$, and $\zeta = 0.7$, and the other at $\xi_0 = -1.8$, $\eta = 1.6$, and $\zeta = -0.7$. The inflow boundary layers were not measurably influenced by the model angle of attack and instead were simply functions of M_∞ and Re_{c_r}.

The boundary-layer rakes have 8–10 pitot tubes within the tunnel wall boundary layer, which extends to $\approx$20 mm (0.08c_r) for all cases tested. The tunnel boundary layers were measured for every run noted in the run matrix, so the actual boundary-layer profiles can be used as input for any M_∞ and Re_{c_r} condition for which the tunnel walls will be modeled as viscous boundaries. The boundary-layer profiles measured along the tunnel walls are standard turbulent flat plate profiles, and simple fits are sufficient to match the velocity distribution quite well.

The actual boundary-layer profiles can be predicted relatively well with a simple two-dimensional boundary-layer code, when the computations include the upstream contraction section of the wind tunnel. A representative result is shown in Fig. 3. The two-dimensional boundary-layer calculations did not include the three-dimensional effects of the contraction section or the effects of compressibility, but these effects are presumably small compared with the uncertainty induced by the location of transition in the contraction section along with the actual distribution of velocity in the section. Indeed, the boundary layers can be matched quite well by simply including a sufficiently long additional flat plate section to the upstream section in the boundary-layer calculations, since the measurement location is hundreds of boundary-layer thicknesses downstream of the contraction section. Note that the effect of finite probe width is clearly evident in the velocity profiles in the measurement closest to the tunnel wall.

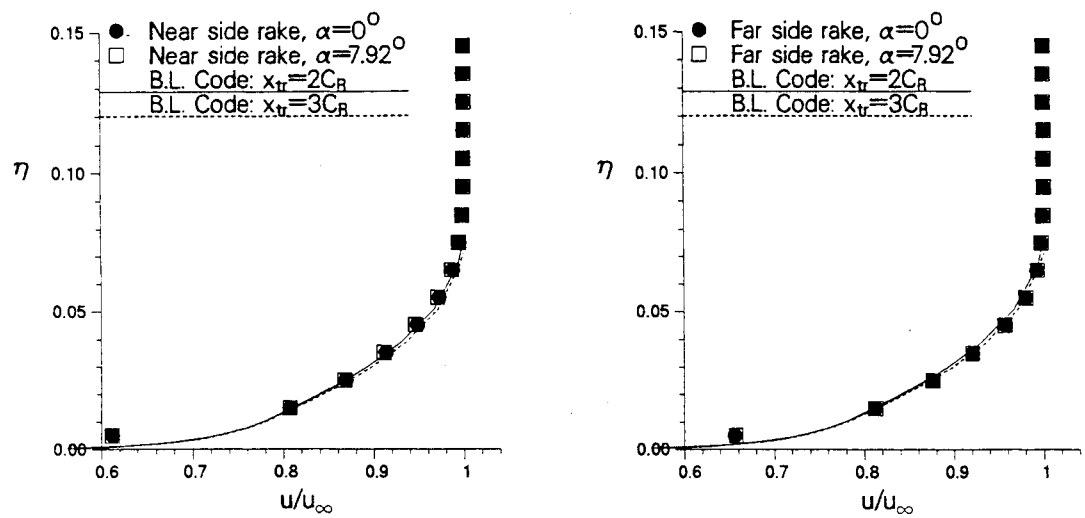

Fig. 3 Tunnel wall boundary layers.

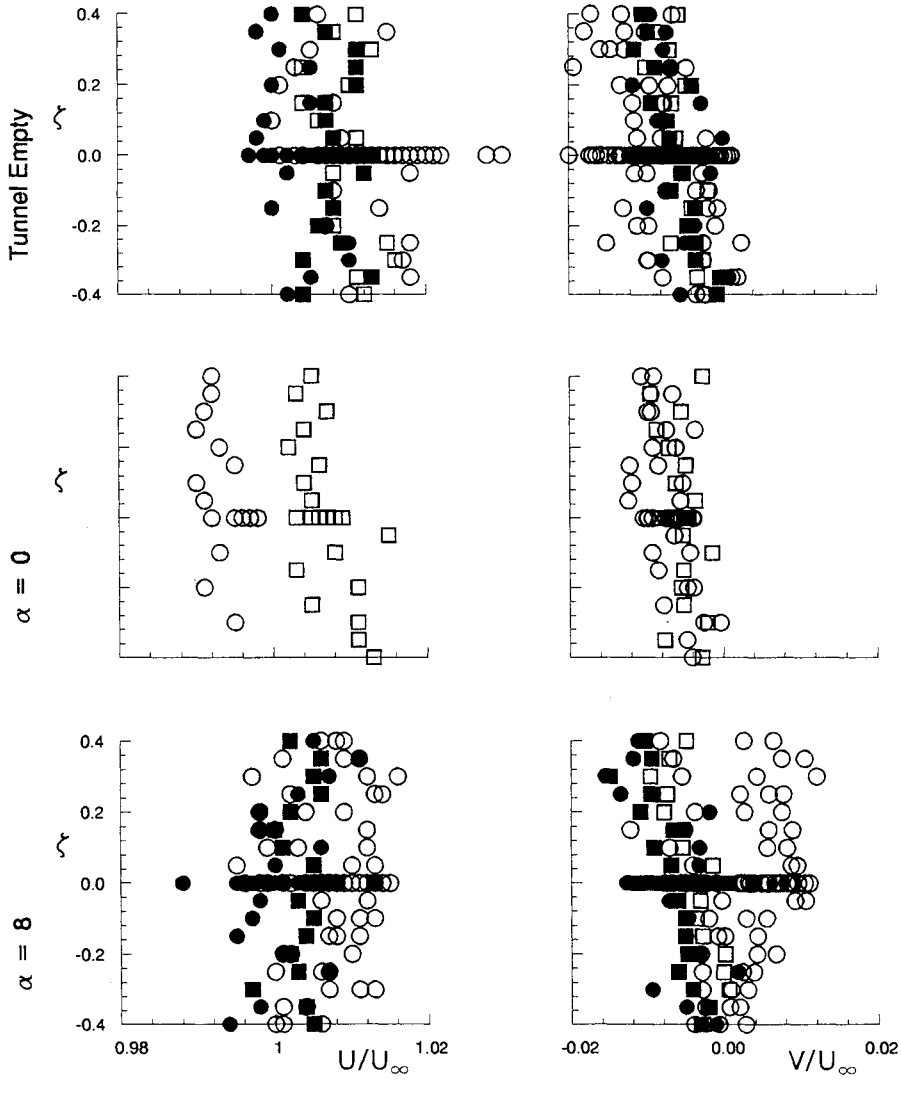

Re_{c_r} (Nominal)	M_∞ (nominal)	
	0.6	0.8
8×10^6	○	□
14×10^6	●	■

Fig. 4 Inflow velocity distribution, $\xi_0 = -1.1$ and $\eta = 0.8$.

Tunnel Core Flow Velocity Measurements

The uniformity of the inflow velocity over the center of the wind tunnel was measured with the laser Doppler anemometer system at $\xi_0 = 1.1$. The velocity was measured in three vertical paths: ¼, ½, and ¾ of the way across the tunnel ($\eta = 0.4$, 0.8, and 1.2). These paths extended from $-0.4 \leq \zeta \leq 0.4$, in steps of $\Delta\zeta = 0.05$. This covers the center one-third of the overall height of the tunnel. The velocities were measured with the tunnel empty and with the model in the wind tunnel at the maximum angle of attack (Fig. 4). The velocities measured were uniform in magnitude to within the accuracy of the instrument, and the flow angularity was 0 deg, again within the accuracy of the instrument. This was the case for tunnel empty, 0 and 8 deg, at low and high Mach numbers and at low and high Reynolds number. As the measurements were made at the extrema of the experimental conditions, the inflow velocities are believed to be uniform at all intermediary conditions of the test, at the inflow measurement station.

Wall C_p Measurements

The tunnel wall static pressures were measured on all four walls. As well as giving a general indication of the influence of the tunnel walls on the flow, the wall pressure measurements also provide a valuable boundary condition for Navier-Stokes codes calculations, in that one can reliably specify the back-pressure (downstream C_p), which will not be zero when there are significant shock waves and/or viscous losses. This has been shown to be important[9] in obtaining correct viscous solutions for other transonic wing flowfields. The wall C_p measurements are indeed far too sparse to provide a boundary condition on the sidewalls, but as the experiment was conducted in a solid wall test section, these boundary conditions are unambiguous without the specification of C_p. These may be modeled as either simple no flow for inviscid walls, or if the computational resources are available, as no slip. The wall C_p measurements then become valuable as a check on the accuracy of the wall modeling treatment. It should be borne in

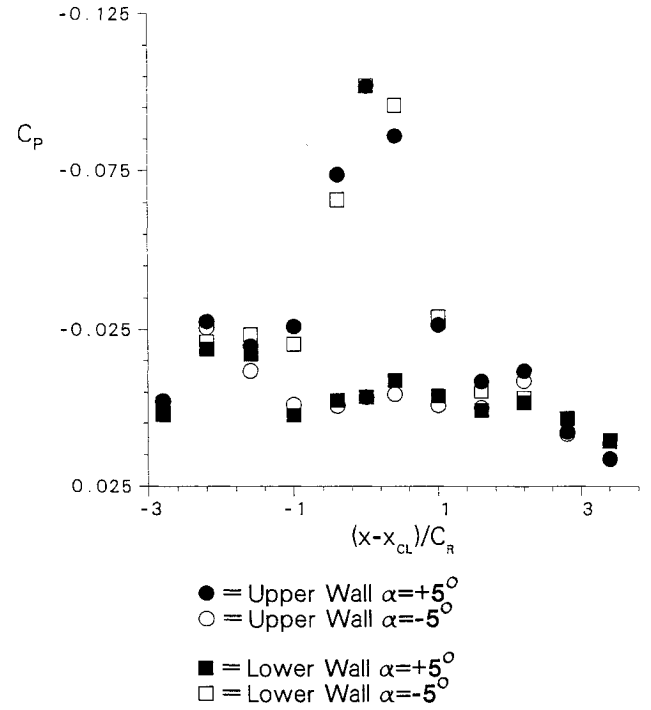

Fig. 5 Wall C_p distribution.

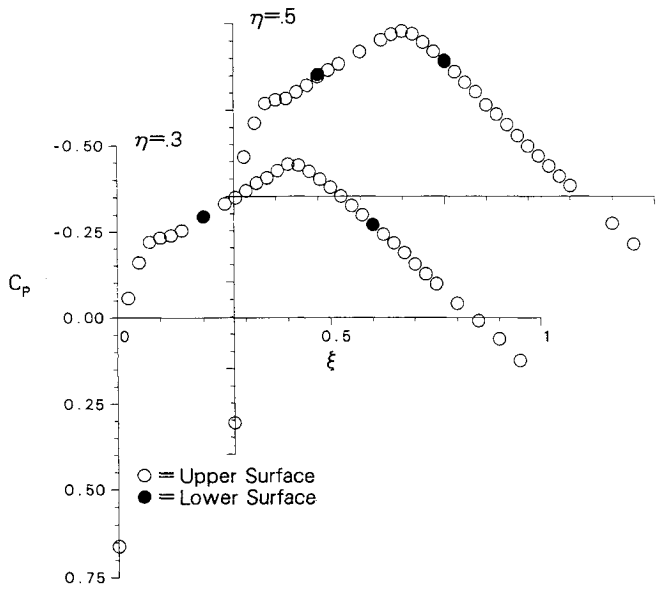

Fig. 6 Upper and lower surface wing C_p.

mind, when doing these comparisons, that the relative error (e.g., percentage) in C_p for these readings is much higher, since the variation in C_p along the walls is slight in comparison with the C_p variation along the wing.

For the lifting cases, the overall lift can be seen in the differences in the upper and lower wall C_p distributions (see Fig. 5). The wall C_p also indicates the magnitude of wall interference in the flowfield. The walls were monitored to ensure that the tunnel was not being choked and that the shock waves emanating from the wing did not extend to the lower or upper walls. A set of wall pressures for one case in which the influence of the walls may have some significance is shown in Fig. 5. For many cases, the influence of the walls will be slight, and simple free air calculations may be adequate.

Wing C_p Results

Model Attitude Determination

The geometric angle of attack was set by using C_p measurements and the symmetry of the experimental geometry. The upper surface of the wing contains 128 pressure taps, and the lower surface contains 4 pressure taps at points corresponding to taps on the upper surface. These four symmetry taps were used to determine the zero lift line ($\alpha = 0$ deg) of the wing.

Given the symmetries of the wing and wind-tunnel configuration, the value of C_p at the lower surface taps should match the C_p values at the corresponding upper surface taps. The wing attitude was adjusted to match the symmetry tap readings as well as possible. The C_p differences after the angle was adjusted were extremely small, less than 0.006 at the condition shown in Fig. 6.

The scatter here is also representative of the scatter that results from setting the angle. Differences of less than 0.1 deg in α produced measurable differences in the wing surface pressures. The geometric angle of attack could be measured to ± 0.03 deg (repeatably). Upper and lower wall pressures also exhibit this level of scatter in C_p spatially (± 0.01 with measurement uncertainties $\leq \pm 0.001$).

At angles of attack not equal to zero, an analogous determination of the zero lift line may be made. The C_p values on the upper surface at positive angle of attack should equal the C_p values on the lower surface at the corresponding negative angle of attack. Similarly, the C_p values on the lower surface at positive angle of attack should match those on the upper surface at negative angle of attack.

The zero lift line determined by adjusting the angle of attack to obtain this correspondence was identical to the line determined for the nonlifting condition, independent of M_∞ and Re_{c_r}, for all α tested. The residual differences in C_p are of the same order of magnitude as in the nonlifting case, 0.006 in C_p.

Note that the precision of this angular measurement is an order of magnitude more precise than that possible with the laser Doppler anemometer system. This implies that the inflow angularity is independent of the flow conditions selected. The difference between the aerodynamic zero lift line and the line of symmetry of the wind tunnel is believed to be caused by the local waviness of the tunnel walls over the model. This difference is indeed measurable but is also slight in terms of its effect on the C_p distributions.

Repeatability of Flow Conditions

The data for lifting cases ($\alpha \neq 0$ deg) were obtained by running the wind tunnel twice for each condition, once with the model at positive angle of attack and once at negative angle of attack. The results from these two runs then provide the data for the suction and pressure surfaces of the wing, respectively. Superimposing the data from two runs in this manner requires careful duplication of tunnel conditions. The extent to which this duplication can be achieved was checked by returning to a given configuration already documented and duplicating the run. This is shown in Fig. 7.

The differences are within the measurement uncertainty, far too small to be discerned from the figure. This indicates that the experiment was well controlled in the sense of Ref. 10.

Analysis of Wing C_p Results

Two small multiple[11] plots are key to this discussion. The experimental conditions form a three-dimensional space whose dimensions are M_∞, α, and Re_{c_r}. If one could take a slice of this space, say along constant M_∞, and look at the C_p distributions on the wing as α and Re_{c_r} vary, then one can get an indication of the overall effect of angle of attack. Figure 8 shows such a cut. In this figure, a single line of plots stretching horizontally shows the C_p for a single α from the inboard station at the left to the outboard station at the right. A single line of plots extending vertically shows the C_p distribution at a single span station, at various angles of attack from $\alpha = 0$

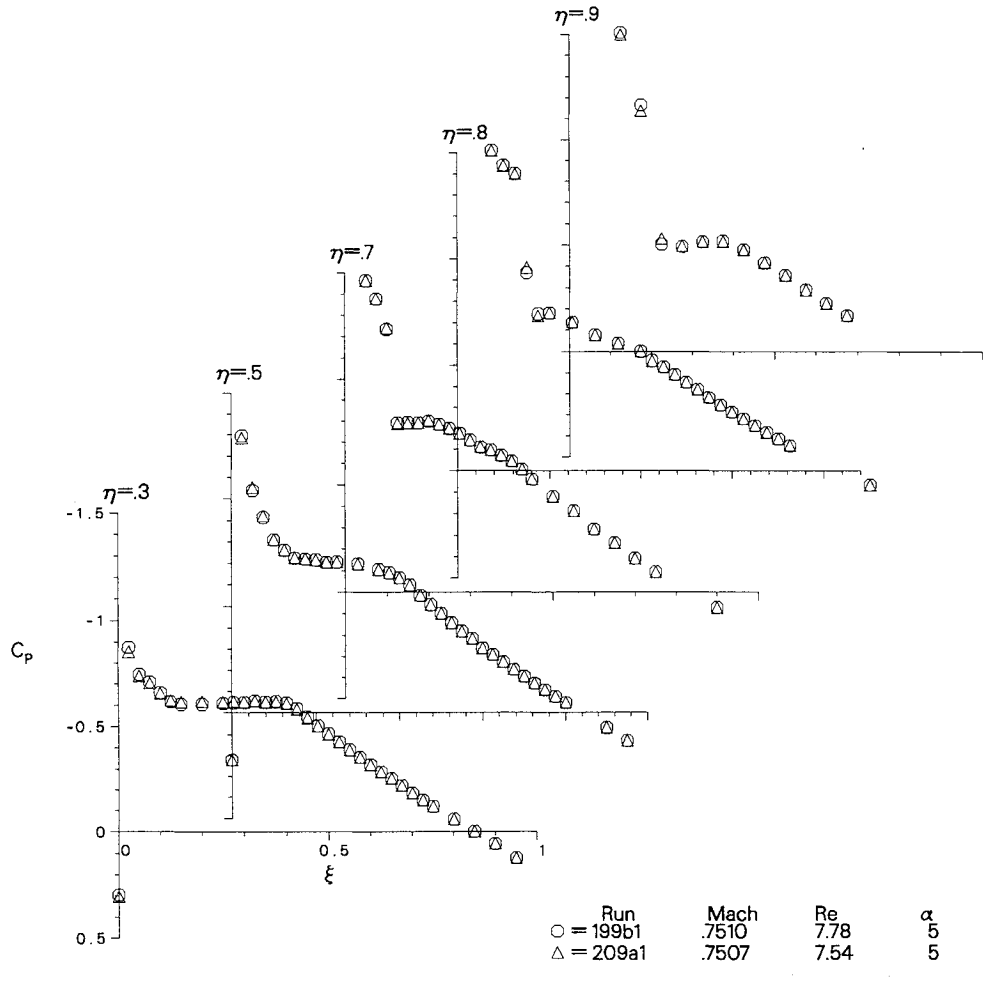

Fig. 7 C_p distribution for repeat runs.

at the bottom to $\alpha = 7.92$ deg at the top. The C_p distribution corresponding to the lower Reynolds number is plotted with unfilled symbols, whereas the higher Reynolds number distribution is plotted with filled symbols. In this manner one can obtain at a glance a view of the multidimensional nature of the data this experiment contains.

It can be seen from Fig. 8 that the relatively low α cases show no appreciable Reynolds number dependence, whereas at the highest α the dependence on Re_{c_r} is striking. It can also be seen that the Reynolds number dependence is more pronounced at the wing tip than at the inboard stations where there is a Reynolds number dependence. Also evident here is the double shock extant for $\alpha = 5$ deg. The line shown in the C_p distributions is not a fairing of the experimental data but rather the predictions of a simple transonic full potential code, TWING, which does not include viscous effects or wind-tunnel walls. The relative fidelity of the predictions of this code at the low angle of attack attests to the small influence of viscous and tunnel walls effects for these cases. It is also evident that the physical phenomena become too complex to predict for this level of code at 5-deg angle of attack and above, at this Mach number.

Another possible slice of the experimental data is to look at the effect of M_∞ on the C_p distributions for a fixed angle of attack. Shown in Fig. 9 is such a view, using again the small multiple plot. In this figure, span still runs from left to right, but here the M_∞ increases as we move up the page. The angle of attack chosen for these C_p distributions was 5 deg.

Here the effect of Mach number can be seen. At the lowest value of M_∞, the Reynolds number effects are again small, and the transonic full potential code is still capable of a reasonable prediction of the flowfield. As the Mach number increases, the Reynolds number begins to make subtle changes to the C_p distribution around the shock, but up to the highest value of M_∞ shown here, 0.775, the differences are relatively minor.

Subsidiary Measurements

The location of transition was believed to be within the first 10% of chord. This estimate is arrived at from the application of grit close to the leading edge in an attempt to trip the flow. The C_p distribution resulting from the trip differed from the untripped distribution close to the trip location and indicated that the grit was simply acting as a bump and not as a trip. Observation of the surface flow patterns with a kerosene/chalk combination also indicated that transition occurred very close to the leading edge, due to the change in the grain size of the chalk remaining on the wing surface. Since the chalk itself could have been acting as a trip, however, this would not be conclusive without the additional information provided by the ineffectiveness of the attempted trip on the clean wing.

Wing deflection was measured at the highest angle of attack. The laser Doppler anemometer system's laser was used as a light pencil, and by bouncing the laser off the wing trailing edge or wing tip, and balancing the reflected light, the laser beam could be positioned at the same position relative to the wing with the airflow on or off. This laser tip deflection (LTD) meter gave estimates of deflections of $0.003c_r \pm 0.0005c_r$ in bending at the wing tip and less inboard along the trailing edge. Since the wing is much stiffer in twist than it is in bending, and the moment loads much less than the lift loads, this bending deflection is the largest deflection undergone by the wing during the test. This deflection is aerodynamically insignificant, based on computations done with TWING, which showed differences between configurations with this amount of dihedral and without much smaller than the other experimental errors.

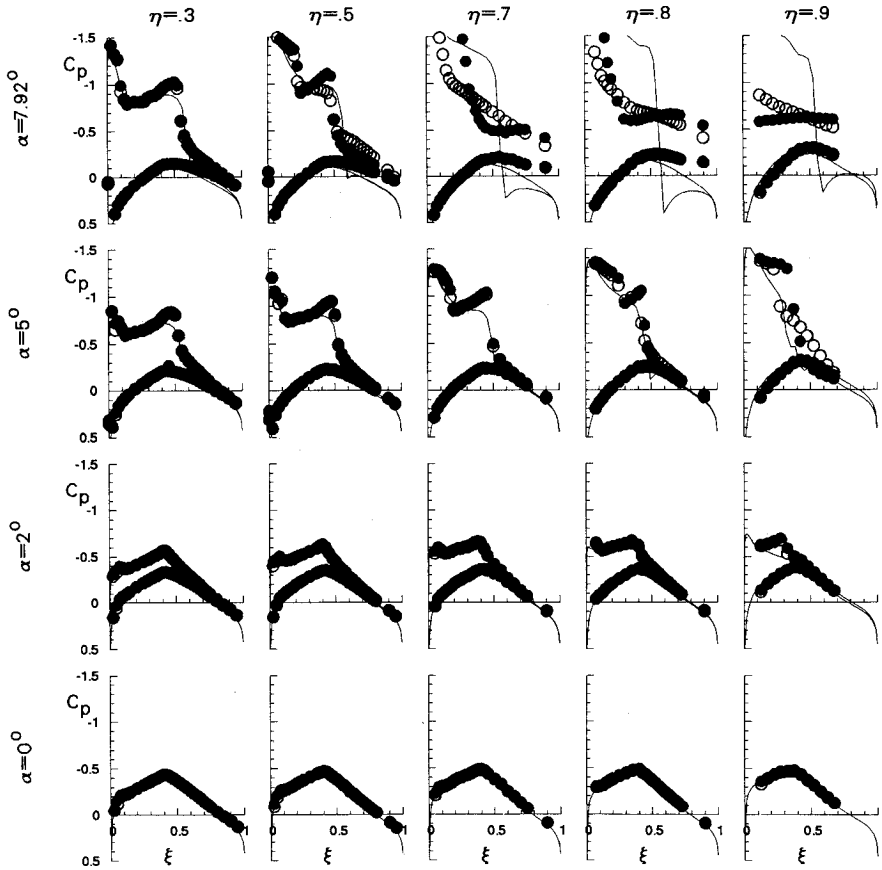

Fig. 8 Wing C_p distribution: α = 0–7.92 deg and M_∞ = 0.8.

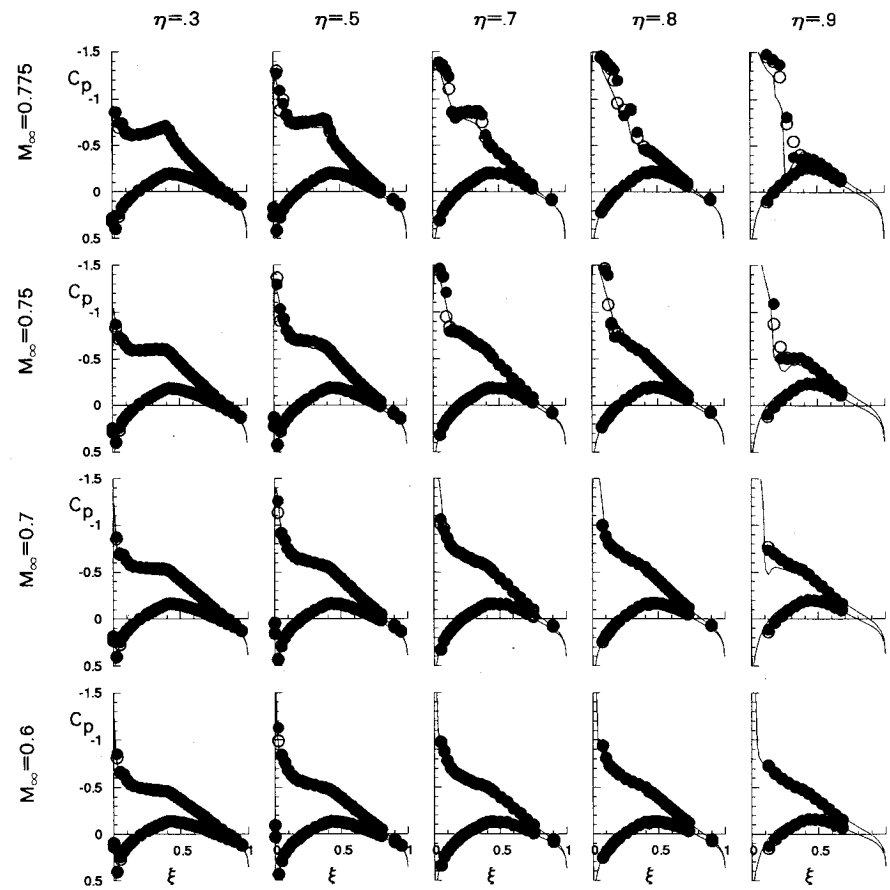

Fig. 9 Wing C_p distribution: α = 5 deg and M_∞ = 0.6–0.775.

Conclusions

The data described here provide a very accurate and complete set of data for validating codes over a range of α, M_∞, and Re_{c_r}. Sufficient data are available to allow boundary (including inflow) conditions to be accurately specified for Navier-Stokes computation. Strict attention has been paid to identifying and quantifying the uncertainty in the experiment.

The flow regimes studied range from very mild subcritical conditions to very extreme viscous flow dominated regimes. The Mach and Reynolds numbers on the experimental model are representative of those at realistic cruise Reynolds numbers. The flow regimes documented include conditions that exhibit repeatable and substantial Reynolds number effects and thus should be valuable in validating time-averaged Navier-Stokes codes.

Acknowledgments

This work was made possible by the efforts of the high Reynolds wind-tunnel operation crew: Bob Wong, C. A. Best, and Victor Horn, mechanics; and Octave Poyadue, electronics technician. The effort required by the exacting nature of this experiment and the amount of time spent ensuring that the data taken were accurate, as well as the attention to detail in the setup and day-to-day operation of the facility, were instrumental in the success of this project. The requirements went far beyond the job description of their positions and required a real team effort to complete successfully. The first author would also like to acknowledge the work of Lionel Levy in the execution of this experiment. He gained a great deal of knowledge through working with L. Levy in this endeavor and enjoyed his inquisitive approach, which served us so well.

References

[1]Marvin, J. G., and Holst., T. L., "CFD Validation for Aerodynamic Flows—Challenge for the 90s," AIAA Paper 90-2995, Aug. 1990.

[2]Marvin, J. G., "Accuracy Requirements and Benchmark Experiments for CFD Validation," *Validation of Computational Fluid Dynamics,* AGARD-CP 437, Vol. 1, Paper 2, May 1988.

[3]Holst, T., "Numerical Solution of Transonic Wing Flow Fields," AIAA Paper 82-0105, Jan. 1982.

[4]Ladson, C. L., and Brooks, C. W., Jr., "Development of a Computer Program to Obtain Ordinates for NACA 6- and 6A-Series Airfoils," NASA TM 3069, Sept. 1974.

[5]Abbott, I. H., and Von Doenhoff, A. E., "Theory of Wing Sections," Dover, New York, 1959, pp. 355.

[6]McDevitt, J. B., Polek, T. E., and Hand, L. A., "A New Facility and Technique for Two Dimensional Aerodynamic Testing," *Journal of Aircraft,* Vol. 20, No. 6, 1983, pp. 543–551.

[7]Seegmiller, H. L., Bader, J. B., Cooney, J. P., De Young, A., Donaldson, R. W., Jr., Gunter, W. D., Jr., and Harrison, D. R., "Development of a New Laser Doppler Velocimeter for the Ames High Reynolds Channel No. II," NASA TM 84367, July 1985.

[8]Benedict, R. P., *Fundamentals of Temperature, Pressure, and Flow Measurements,* 2nd Ed., Wiley, New York, 1976, pp. 343–371.

[9]Kaynak, U., Holst, T., Cantwell, B. J., and Sorenson, R. L., "Numerical Simulation of Transonic Separated Flows over Low Aspect Ratio Wings," AIAA Paper 86-0508, Jan. 1986.

[10]Moffat, R. J., "Contributions to the Theory of Uncertainty Analysis for Single-Sample Experiments," *1980–91 AFOSR-HTTM-STANFORD Conference on Complex Turbulent Flows,* Stanford Univ., Stanford, CA, Vol. 1, pp. 40–57.

[11]Tufte, E. R., *Envisioning Information,* Graphics Press, Cheshire, CT, 1990, pp. 66–79.